A methodology to obtain the single lap shear allowable strength of thermoplastic polymer composites by a validated modelling and simulation approach

J. Ninyerola Gavaldà[a,*], I. R. Cózar[a], J. M. Guerrero[a], S. Abdel-Monsef[a,b], A. Sasikumar[a], A. Turon[a,*]

[a] *AMADE, Polytechnic School, Universitat de Girona, Campus Montilivi s/n, 17003 Girona, Spain*
[b] *Structural Engineering Dept., Faculty of Engineering, Zagazig University, P.O. Box 44519, Zagazig, Sharkia, Egypt*

Abstract

Although there exist several modelling approaches to simulate the strength of the single lap shear configuration, the application to obtain design allowables has not been addressed. Moreover, the determination of design allowables by simulation needs to be sustained by a feasible modelling and simulation approach, demonstrating their ability to propagate uncertainties. In this paper, we present a structured methodology to validate a modeling and simulation approach for the forward propagation of parameter uncertainty. This methodology is applied to determine the single lap shear allowable strength of a thermoplastic carbon fiber composite. The defined approach, which involves advanced damage models, has been validated through a dedicated test campaign. We analyze the influence of batch size on the validation process and the prediction of allowable strength. The results obtained demonstrate the feasibility of obtaining design allowables by simulations.

Keywords: Uncertainty Quantification and Management, A. Thermoplastic resin, C. Finite element analysis (FEA), B. Strength, C. Statistical methods

1. Introduction

Lightweight materials, like carbon fiber reinforced polymers (CFRPs) are increasingly used in designing aircraft components due to their high specific stiffness and strength. However, one of the major drawbacks lies in recycling thermoset polymer (TS) matrices used in CFRPs, as they are difficult to separate at the end of an aircraft's life [1, 2]. To address this, the aerospace industry is exploring thermoplastic matrices (TP) for CFRPs, which can be melted and separated, enhancing recyclability and end of life considerations [2–7].

Recent studies have shown that CFRPs with thermoplastic matrices (TP-CFRPs) have superior material properties compared to those with thermoset matrices (TS-CFRPs) [8, 9], for matrix dom-

*Corresponding author. Tel.: +34 972 41 88 17.
Email addresses: joan.ninyerola@udg.edu (J. Ninyerola Gavaldà), albert.turon@udg.edu (A. Turon)

inated failure mechanisms. TP-CFRPs allow for the production of lighter components, providing a significant advantage over TS-CFRP.

Unlike other materials, manufacturing processes for CFRP components are complex and may lead to variability, defects, flaws, and misalignment, which may have an impact on the design properties, thus compromising the reliability of the structure [2–7]. Therefore, to minimize risks and ensure safety, the certification bodies define regulations and demands the implementation of a meticulous certification process. The existing certification and qualification method for airframe structures is nowadays based on experimental testing campaigns following a pyramid of levels, commonly referred to as the building block approach (BBA) [10]. This methodology places a strong emphasis on conducting physical tests at lower pyramid levels to systematically quantify the uncertainty of the material properties to define material allowables and, based on the material allowables and on specific loading conditions, obtain the design allowables (DA), which are subsequently used for sizing.

The DA for CFRP components are defined as the basis values. A-basis value (A-value) is typically required for primary load-carrying structures and B-basis value (B-value) for strucutres with redundant/multi-load-path. The basis values can be determined experimentally following the guidelines provided by the CMH-17 [11]. The determination of the A-value is more demanding, requiring at least 75 specimen results compared to the 30 (referred to as robust sampling) needed for the B-value under the same approach and 18 for the reduced sampling approach [11].

The requirement for a high number of samples in an exhaustive experimental campaign contributes to an expensive and time consuming procedure. As a consequence, the ability to fully exploit the weight-saving potential offered by advanced composite materials is limited due to the low reliability of the DA when only a few specimens are tested. In addition, these extensive and time consuming experimental campaigns can significantly complicate the entry of the next generation aircrafts with disruptive technologies into the service. Consequently, this conservative stance may not allow for the full optimization of the structure for weight savings, thus running counter to the objectives of Clean Aviation program [12] and negatively impacting fuel consumption.

As a result, advancing methodologies to enhance the reliability of generated DA could prepare for a cost-effective, efficient and faster certification and qualification processes in airframe structures. In recent years, methodologies employing numerical approaches for obtaining DA have emerged based on non-deterministic approaches. For instance, Vallmajó et al. [13] introduced a semi-analytical approach, and Furtado et al. [14] expanded on this work by integrating machine learning algorithms.

While semi-analytical approaches catch attention due to their significantly lower computational time compared to high-fidelity models (HFMs), their applicability is limited by a constrained domain of validity. Therefore, addressing challenges in more complex loading scenarios or situations lacking a semi-analytical model involves employing finite element (FE) simulations. Nam et al. [15] estimated DA for unnotched and open-hole laminates under tension using FE simulations. Catalanotti [16] confronted with the same issue, incorporating a more advanced progressive damage model for FE simulations and employing a machine learning approach with bootstrapping, for enhanced prediction efficiency and reliability. For intricate loading scenarios, Cózar et al. [17] generated A/B-values through a HFM for a combination of low-velocity impact and compression-after-impact tests accounting for input parameter uncertainties.

However, the determination of single lap shear (SLS) strength allowables through simulation remains unexplored. Despite numerous studies in the literature exploring the simulation of SLS strength using HFMs — either relying only on cohesive elements [18–20] or incorporating a progressive damage model for laminate failure [21] — a non-deterministic validation of these simulation approaches is not enough developed.

The deterministic validation of the numerical methodology encompasses both qualitative and quantitative evaluations. On a qualitative level, a comparison can be made between the deformation of an experimental sample during testing, the shape of the load displacement curve and the failure mode against the predictions of the HFM. In quantitative terms, the average failure strength derived from experimental data can be compared with the failure strength predicted by the HFM as done by Fatemi et al. [22].

However, a deterministic HFM alone is insufficient to incorporate the uncertainties inherent in the manufacturing process and the experimental tests procedure. To address this, it is imperative to define a modeling and simulation (M&S) approach that involves HFM and can account for and propagate these uncertainties [23]. The non-deterministic validation becomes crucial to account for uncertainties and to compare with the dispersion observed in the experimental data.

Some research attached the intrinsic deterministic behavior of the HFM by propagating the dispersion of the experimentally obtained results by the statistical technique of design of experiments (DOE) [24–26] generating what is know as forward modeling and simulation approach. The DOE consist of a methodology for the generation of different values, following a specific strategy, which permits to be taken into account the characteristic of the existent data. Thus, the forward M&S approach consist in running multiple simulations of the same model with different combinations of the input values generated in the DOE. Some examples of the application of forward M&S by the application of DOE in the generation of the SLS strength, is the work done by Da Silva et al. [27, 28] to quantify the influence of the adhesive, adherent and geometric parameters of the SLS test. Rangaswamy et al. [29] predicted by DOE and neural network approach the impact of the overlap length and the adhesive thickness in the SLS test. However, a comprehensive validation of the forward M&S approach for being reliable to predict DA has not been addressed. Some efforts were done by Joannès et al. [30], by studying the influence in the measurement of the uncertainty and due to the sampling randomness fitting the experimental results with a 2-parameters Weibull distribution in the fibre strength. However, the validation remains incomplete, since only a deterministic comparison of the error in the parameters and in the results obtained from them was performed.

Some other researchers developed a forward M&S approach propagating the uncertainty and validating in multi-scale simulations approaches. As Tao et al. [31], who based in Representative Volume Element (RVE), for woven composites, generated Statistical Representative Volume Elements (SRVE), surrogate models and experimental tests to address the simultaneous uncertainties at micro-scale, meso-scale and macro-scale respectively following a Gaussian distribution for all the inputs. They validated the model by the error average between SRVE and analytical equations in micro-scale, cross validation in meso-scale and the error average between SRVE and the experimental results. Zhang et al. [32] proposed also a physically based multi-scale approach for the uncertainty quantification of hybrid aluminum-CFRP riveted or bonded lap joints propagating the distribution of the experimental data. Despite the fact the validation is based on the comparison between experimental and numerical distributions, the validation of is based in the comparison of the error between the statistics of the distributions, non taken profit of the multiple data generated for a non-deterministic validation.

Catalanotti [33] propagate the uncertainty of the material properties through bootstrapping, followed by Markov Chain Monte Carlo methods which combined with Bayesian analysis, permits to determine the distribution of a QoI. The distribution is validated by the Gelman-Rubin index, which check when a Markov Chain is stationary (criterion for a valid distribution following Markov Chain methods). Catalanotti's approach optimizes the statistics of the QoI distribution by restricting the optimization to a single type of distribution, thereby limiting the flexibility of this approach. Finally, the validation of the numerical approach is done by the comparison between the experimental results and the DA numerically generated.

Another proposed approach is the inverse M&S, in which the uncertainty in the well known results are propagated to obtain the uncertainty in the material properties used in the model. Ciampaglia used this approach in [34] for calibrating the SRVE for different scales based on the experimental results obtained with DIC in a tensile test.

As can be seen, the validation of the uncertainty done in the studies presented is based on the deterministic error comparison between the experimental average data and nominal HFM results or, as maximum, a non-deterministic validation consisting in the error quantification between the statistics of the distributions obtained.

It is not the case of Fatemi et al. [22, 35] and Poort et al. [36] which applied the area metric (Roy et al. [37]) in a non-deterministic validation of the uncertainty between the experimental results and the numerical models to forward propagate uncertainties at different levels of the BBA pyramid. The area metric quantifies the dissimilarity between the distributions of two samples, providing a more accurate comparison than traditional error metrics by considering the entire shape of the cumulative distribution function (CDF). In addition, this approach enhances the comparison between different types of distributions.

Thus, the validation of a M&S approach based on the forward uncertainty propagation of the material properties must be conducted using a non-deterministic approach, with the area metric as a criterion for the validation after the deterministic validation of the nominal HFM. For this reason, the primary goal of this paper is to propose a non-deterministic validation methodology for a forward M&S approach, involving HFM, to assess the single lap shear strength. For the validation, a DOE is executed to capture the random results dispersion, essential for a statistical analysis of simulation outcomes. The statistical distribution and relevant metrics are calculated from experimental data for each input parameter in the HFM, following the process outlined in CMH-17 [11].

Deterministically, comparisons involve examining load-displacement curves and the B-value of the SLS strength, calculated from both experimental tests and simulation. Non-deterministically, the disparity between methodologies is assessed quantitatively. Statistical tests are employed to qualitatively compare data distributions from the experimental testing campaign and the simulation-generated data. This comparison is executed across various sizes of numerical batches to determine the minimum size required for comparable results between numerical and experimental approaches. Additionally, the comparison is repeated to obtain the dispersion of the DA strength, providing discernment about the reliability of quantification of DA by simulation compared to the experimental procedure.

The paper is organized as follows: first, we present the details of the experimental test campaign. Subsequently, we outline the M&S approach employed for computing DA. Following that, we present the results of the experimental test campaign, accompanied by both deterministic and non-deterministic validations of the M&S approach. We also explore the impact of sampling size on the reliability of DA predictions. Lastly, we engage in a comprehensive discussion leading to the main conclusions drawn from this work.

2. Methodology to validate the Modeling and Simulation approach

The methodology to validate the M&S approach to be afterwards used to obtain the DA is presented here. As outlined in Fig. 1, a two-step validation has been performed. First a deterministic validation of the M&S is performed, by comparing the quantity of interest (QoI) obtained using the HFM with the nominal values of the material card against the average experimental QoI. A non-deterministic validation is then followed by comparing the statistical distribution of the experimental data with a set of simulations forward propagating the random uncertainty on the material parameters.

2.1. Deterministic Validation

The deterministic validation of the M&S consists in running the HFMs with the average values for the material properties (nominal values) needed as the input parameters, to afterwards, compare the QoI obtained from the simulation with the experimental data. The a-priori criteria used is that the difference between the HFM simulation and the average of the experimental data to the corresponding displacement levels has to be within a predefined bound (a tolerance). Moreover, for a qualitatively validation, the strain contour of the HFM computed is also compared with the strain contour measured in the experiments using Digital Image Correlation (DIC), validating the suitability of the HFM within the M&S approach.

2.2. Non-deterministic validation

To perform a non-deterministic validation, a batch of specimens with different input values is generated by a Monte Carlo sampling method based on the statistical distribution of the different inputs parameters of the M&S approach to forward propagate the aleatory uncertainty of the material properties. Initially, the average QoI and the defined confidence interval range are calculated from the numerical simulations and are compared with the experimental data. Secondly, a comparison between the distributions of the QoI for both cases (numerical and experimental results) is carried out.

We propose to compare the CDF from M&S approach with the CDF from the experimental test campaign. From the obtained results, the empirical CDF (ECDF) is computed for both cases (M&S and experimental) and to be able to compare the difference between ECDF with an a-priori criterion for evaluation, a validation metric based on the area between the two CDFs is defined, using the expression

$$\%d_{Area} = \frac{100}{\bar{x^e}} \int_{-\infty}^{+\infty} |F(x^s) - F(x^e)| dx \tag{1}$$

where $\bar{x^e}$ is the average value of the QoI for the experimental data, $F(x^s)$ is the predicted QoI ECDF of the M&S results and $F(x^e)$ corresponds to the ECDF from the experimental data, wherein smaller values signify a similarity between distributions. However, even small $\%d_{Area}$ below the bound defined can not certify that the distributions compared are similar particularly at the tails of the distribution.

The difference between the ECDF of the M&S approach and that of the experimental data can be classified into four different scenarios (see Fig. 2). Scenario 'a' (ideal scenario), where the distributions are the same, as reflected by the same length and scale. However, the probability of being in 'scenario a' is really small, specially when the available data for the QoI is limited and the obtained distribution is susceptible to drastic variations with any new result. Thus, there will be differences in shape and location between both ECDF most of the times. This circumstance does not allow to determine in which scenario we are simply by comparing the statistics of the distributions.

Hence, it is necessary to define an interval of confidence for the validation of the similarity between ECDF. Hypothesis validation tests permit to compare the similarity between distributions by taking into consideration an interval of confidence. For this reason, hypothesis validation tests are the last step of this methodology –if both distributions are similar ('scenario a'). We propose Kolmogorov-Smirnov (KS) [38], Anderson-Darling (AD) [39] and Cramer-Von Mises (CV) [40] because are appropriate for empirical comparison of CDF.

If, with the p-value corresponding to the confidence interval a-priory defined as the criterion, the hypothesis validation tests do not find enough difference between ECDF, we are in 'scenario a' in Fig. 2. However, if the statistical tests are rejecting the similarity between ECDF, it does not necessarily mean that we are in 'scenario d' (worse case and not validated in this methodology). Two more scenarios (scenarios 'b' and 'c') are taken into consideration in this moment and, depending in which scenario we are, the criterion used for the DA generation could be affected.

First of all, we propose to apply an offset equal to the distance function known as Wasserstein metric (W_p) in the numerical results, resulting in a similar location for those distributions that initially do not pass the hypothesis validation test and perform the statistical test again. For the case of one-dimension distributions, W_p is defined as

$$W_p(\mu_1, \mu_2) = \left(\int_0^1 |F_1^{-1}(q) - F_2^{-1}(q)|^p dq \right)^{1/p} \tag{2}$$

where $F_1^{-1}(q)$ and $F_2^{-1}(q)$ are the inverse of the CDFs from the numerical and experimental results, respectively, and p is related to the moment of W_p. The offset is calculated for p = 1 (W_1), which represents the expected value for the distance between functions.

If after the offset application the null hypothesis is not able to be rejected, it is confirmed that the scale of the distribution is similar. Therefore, we are in 'scenario b'. Taking into consideration that the error between average of the distribution for the M&S approach is already validated in the previous step, we assume the 'scenario b' as validated and do not have more inference than the initially accepted tolerance defined in the average comparison, in the DA generated.

When the null hypotheses is rejected after the offset application means that the scales of the distributions differ too much to be the same distribution (scenarios 'c' and 'd'). Even if the averages of the distributions are similar ('scenario c'), multiple distributions can be generated with the same location generating different effects in the DA a-posterior generated. Therefore 'scenario c' is not validated and together with 'scenario d', the authors recommend to improve the M&S strategy before DA generation for these two scenarios.

Finally, if the M&S approach is validated, it is considered credible to propagate the aleatory uncertainties of the material properties and calculate statistical quantities, such as the B-value.

2.3. Influence of the batch size

In addition to the validation of the M&S strategy, the influence of the batch size is also analysed. Different batch sizes have been used to validate the M&S approach, to afterwards compute the B-value. The Knockdown Factor (KDF) [41, 42] is used to analyze the influence of batch size on the reduction of allowable strength compared to the average value. It quantifies the difference between the average strength and the B-value for the two approaches studied in this paper (M&S and experimental):

$$KDF = \left(\frac{B}{\bar{x}}\right) \tag{3}$$

where B represents the B-value obtained for each generated batch and $\bar{x}$ is the average result from the total sample size in each studied approach in each case.

The strategy is implemented as follows: from the initial population derived from the M&S approach, a large number of random selections (n) have been conducted for batch sizes. Each batch generated was subjected to non-deterministic validation and the B-value is extracted. Finally, the KDF was calculated and the average along with the 95% confidence interval of the KDFs were calculated for each batch size. Simultaneously, the Bootstrap method [43] is employed to assess result dispersion across the entire population, given the limited data available for generating dispersion results with the total population size.

The use of a large number of iterations allowed for the generation of a substantial sample size, contributing to the study's reliability. This approach facilitated more precise estimations of population parameters, reducing random variability and enabling the identification of infrequent outcomes, such as data converging into a log-normal distribution—a rarity in B-value procedures. Using the results obtained from the non-deterministic validation conducted for each batch, a comparative analysis of the different tests employed to validate the obtained dispersion is performed across various batch sizes. The aim is to identify the minimum batch required for the non-deterministic validation of the M&S approach implemented for this particular case study.

3. Case study: Singe Lap Shear configuration

This section extensively outlines the case study analyzed: the SLS configuration, the manufacturing procedure used to generate SLS specimens from TP-CFRP, as well as the approach employed to experimentally obtain the allowable shear strength.

The SLS tests followed the AITM 1-0019 Airbus internal standard [44]. A quasi-isotropic panel comprising 32 plies, arranged in the stacking sequence $[(0/45/90/\text{-}45)_{2s}/(0/45/90/\text{-}45)_{2s}]$ was manufactured through hot pressing with a thermoplastic material, resulting in a final arm thickness of 5.28 mm. The manufacturing process done by INEGI (Porto, Portugal) and the material supplier, consisted of four steps: (i) The panel was heated from the room temperature until 150 ºC at 5 ºC/min at 1 bar, and then the pressure increased to 10 bar until the consolidation temperature of 390 ºC was reached; (ii) the temperature was kept for 1 hour while maintaining the pressure at 10 bar for the consolidation process; (iii) the panel was cooled down at -5 ºC/min and 10 bar (fast crystallization) until 150 ºC, and then the pressure decreased to 1 bar and the panel cooled to room temperature; and (iv) the panel was inspected with a C-Scan.

The SLS specimens were obtained by precisely machining the slots in the consolidated panel with a 12 mm overlap between arms and a 1.6 mm gap on each side, see Fig. 3a, and then cut to their final geometry, resulting in a final arm thickness of 2.64 mm with the stacking sequence $[0/45/90/\text{-}45]_{2s}$ on each arm. The overall length of the specimens was 110 mm. The width of the specimens was 25 mm and a 20 mm lengthwise section on each side of the specimen was utilized to secure the specimen with grips to the testing machine.

3.1. Experimental methodology definition

Tensile lap shear joint tests consist on applying a tensile load in the axial direction of the specimen (x-axis in Fig. 3b). During the test, the tensile loading is transferred from one arm to the other through the bonded region between the upper and lower arm. At a certain load, typically debonding starts from the gap region. The SLS strength is obtained dividing the peak load by the cross section bonded area (see Eq. (4)). Depending on the material properties and the laminate stacking sequence, ply failure can undergo. However, the SLS specimen configuration was chosen to minimize the possibility of ply damage before the loss of adhesion between arms [45, 46] as can be seen in Fig. 3c.

The experimental test campaign was conducted at AMADE lab facilities, following the AITM 1-0019 standard [44]. A displacement controlled test at a speed of 0.25 mm/min was applied. The resulting load was recorded by a calibrated load cell and a 2D DIC technology was employed to record the displacement of the specimen's edge.

One edge of the specimens was painted with a white background and a random black speckle pattern in front, which allows the software Vic-2D 2009, developed by Correlated Solutions Inc., to track the displacement based on pictures of this edge. The pictures were taken every half second with a camera with a 2/3 inch CCD sensor installed providing 14-bit grey-scale images of 5 megapixels. The area of interest was approximately 15 mm in length by the thickness of the specimen, and the pictures were taken at a distance of 500 mm of the specimen, with a focal length of 60 mm, and a lens aperture size of f/11 to avoid distortion in the limits of the lens [47]. The selection of the lens was based in the MachVis software. The software setup for image correlation involved a subset of 21 for the selected reference point, with 10 steps, and the studied area encompassed the overlap area plus an additional 20 mm on each side. In the analysis, the interpolation was optimized using a 4-tap method, and the low-pass filter images option was activated. For displacement correlation, points were selected near the edge of the specimen, specifically 10 mm after the gap, for both arms (blue points in Fig. 4). These points were strategically chosen because their displacement is barely affected by the fracture process zone, and the specimen's rotation in this region is smaller than in the rest of the area of interest. To address potential inaccuracies due to the onset and propagation of a crack in the bonded area, the final displacement studied in this research is the difference in the x-axis of this 2 points, mitigating displacement errors related to the presence of a crack by subtracting the deformation of the fixed arm.

The failure strength was defined as

$$\tau_{SLS} = \frac{F}{WL}, \tag{4}$$

where F is the load recorded by the load cell, W is the width of the specimen and L is the length of the gap.

The SLS strength allowable was defined as the B-value, which depending on the distribution of the existent data is obtained following the procedure defined in the CMH-17 [11]. For example, if the existing data follows a normal distribution, the B-value can be calculated as

$$\tau_B = \bar{\tau}_{SLS} + K_b s_{SLS}, \tag{5}$$

where $\bar{\tau}_{SLS}$ and s_{SLS} are the mean and the standard deviation, respectively, of the measured SLS strengths, and K_b is a parameter that depends on the number of tested specimens as defined in [11].

3.2. Modeling and Simulation approach

The M&S approach used for simulating the SLS test consists of an explicit model generated in Abaqus software [48]. After calibrating the model, it employs 3D reduced integration solid elements (C3D8R) to represent the geometry of the model, with one element through-the-thickness per ply. In addition, aiming to accurately simulate the behaviour of the specimen (delamination in the bonded area), the interface between both arms is defined with cohesive elements (CE) of 0.001 mm of thickness (see Fig. 5). The physically based cohesive zone model developed by Turon et al. [49] is employed in the present work. The in-plane element size of the cohesive elements is defined to ensure a minimum of two elements spanning the fracture process zone [50], which is calculated following the procedure described by Soto et al. [51] (approximately 0.1 mm). The displacement is fixed in the lateral face of one arm and in the opposite side a tensile displacement, at low velocity to prevent kinetic effects, is applied (see Fig. 5). The model is defined by ten input material properties, all derived from experimental test campaigns, linking the validation of the model to accurate data acquisition and uncertainty quantification. The exception is the penalty stiffness (K), which is calibrated to avoid influencing the compliance of the resulting behavior [50]. The effect of geometrical variability was not considered in this work. The variability in the geometrical dimensions of the specimens was measured to be very low and, therefore, was not included in the forward problem.

3.3. Material card definition

The material system is AS7/PEKK. A specific test campaign to obtain the statistical distribution of the different material properties was performed. As the SLS specimens, the specific specimens needed in the material characterization for each test were manufactured by INEGI and the material supplier. The experimental test campaigns were performed at AMADE lab. The elastic behaviour of this material is defined with 6 material properties: the Young's Modulus in fibre and matrix direction (E_{11}, $E_{22} = E_{33}$), the Shear's modulus ($G_{12} = G_{13}$ and G_{23}) and the Poison's ratios ($\nu_{12} = \nu_{13}$ and ν_{23}). The material parameters were experimentally obtained from a specific test campaign developed in our lab facilities following the appropriate standards [52–58], except for the transverse Poisson's ratio (ν_{23}) which was assumed equal to 0.45 [59, 60]. Similar values ν_{23} were experimental measured for a thermoplastic-based composite material in [61]. The Shear's modulus G_{23} is calculated as

$$G_{23} = \frac{E_{22}}{2(1+\nu_{23})}. \tag{6}$$

The six cohesive model parameters required to define the behavior in the bonded region are: the critical fracture toughness and failure strength under mode I ($\mathcal{G}_{Ic}$, τ_I^0, respectively) and mode II ($\mathcal{G}_{IIc}$, τ_{II}^0, respectively), the B-K constant (η) and the penalty stiffness. The fracture toughness in mode I is obtained from the Double Cantilever Beam (DCB) test [55], while G_{IIc} is measured from the End Load Split (ELS) test [56]. In both tests, the fracture toughnesses were obtained using the inverse method developed by Said et al. [57, 58]. This method generates a cohesive law from the load-displacement curves obtained from the respective tests. The value of the Benzeggagh-Kenane (η) was extracted from the experimental mixed-mode bending (MMB) delamination test, carried out following the standard [54]. Finally, the penalty stiffness used in the cohesive zone model is fixed as 10^6 N/mm^3. More details about the number of specimens tested, the tests and standard used for the data reduction are provided in Table 1.

3.3.1. Uncertainty Quantification for material card test parameters

The aleatoric uncertainty of the data from the test campaign to obtain material properties required for the model was evaluated following the procedure described in [62]. The Anderson-Darling test [40] was performed sequentially for Weibull, normal, and log-normal distributions. If the observed significant level (provability that the data are actually from the distribution being tested) was greater than 0.05, the tested distribution is accepted as correct (with a maximum error of 5%). Table 1 provides the test and data reduction method, along with the statistical distribution for the different input material properties.

The scale parameter of the distribution (scalar statistic parameter) was normalized with respect to the experimental average value of each material property due to confidentiality agreements with the material provider. For all the material properties studied, the mandatory initial distribution checked (Weibull distribution) was validated, and thus no other distribution was considered, as defined in [62]. For all the properties evaluated the Weibull distribution was selected.

4. Results

4.1. Deterministic Validation

To quantitatively validate the modeling and simulation methodology in a deterministic manner, the load-displacement curve obtained from the deterministic numerical result was compared with the average experimental one, defining an a-priori bound for the validation of the average results.

Five representative values have been studied in this study. Initially, the normalized load for the following corresponding displacement points: u_{60} representing the 60% of the maximum normalized displacement, where the curve is still in the elastic range in which no damage is observed in the specimen; u_{80} representing the 80% of the total displacement, approximately marking the inflection point where the damage reduces the slope of the curve; u_{90} representing the 90% of the maximum normalized displacement, located midway between the onset of damage and the failure strength of the specimen; and u_{100} representing the maximum normalized displacement achieved (see Fig. 6). Finally, the last representative value compared is the normalized slope of the elastic part of the test.

Note that the results presented in Fig. 6 are normalized by the mean of the maximum load or maximum displacement, respectively of the experimental test specimens for confidentiality agreement with the material supplier. Therefore, the slope of the elastic region computed is adimensional. A summary of the values obtained, together with the difference between the numerical and experimental data, is provided in Table 2.

For the deterministic case, the difference in the normalized elastic slope and for the normalized load at point u_{60} is higher in comparison to the loads at points u_{80}, u_{90} and u_{100} represented in Fig. 6. This is due to the fact that the load achieved at the beginning of the experiments is higher than the numerically predicted, generating a higher slope in the elastic range than in the nominal numerical model. This difference is finally compensated by the decay of the experimental curve, which starts before than in the numerical case. Despite of these differences between the HFM and the experimental specimens, the differences obtained are lower than the a-priori defined criterion of 5%.

The strain field obtained during the fracture process with the nominal result for the HFM is compared with the correlated image from a experimental specimen. Logarithmic strains are obtained in the length direction of the specimen (x-axis) using DIC technology as illustrated in Fig. 7. In the examination of both numerical and experimental assessments presented in Fig. 7, a consistent pattern between the experimental specimen and the HFM is evident throughout all investigated points in this study. This observed behavior aligns with the anticipated characteristics of a SLS test [63, 64]. Specifically, a preliminary trend is discernible prior to the onset of damage (denoted as point u_{60}), wherein a positive strain manifests near the cohesive surface, indicative of the subsequent crack propagation. After to the crack initiation, strain values escalate uniformly across the remaining data points, maintaining a correlation between the numerical model and experimental test outcomes. Comparing the general behaviour of both approaches it can be seen that the contact surface between arms act as a plane of symmetry in both cases and the delamination in both cases occurred in this part of the specimen. Thus, qualitatively, it is possible to validate that the strain contour predicted by the HFM is in good agreement with the experimental one, despite of the assumptions done in the HFM.

Simultaneously, an analysis of the relationship between ratio of damage dissipated (r) in the cohesive elements and strain was conducted for the HFM. This examination is depicted in Fig. 8. r is defined by Turon et al. [49] as

$$r = \frac{\mathcal{G}_d}{\mathcal{G}_c}, \tag{7}$$

where $\mathcal{G}_c$ is the total energy per surface area needed to develop all the degradation of the interface and $\mathcal{G}_d$ is the current dissipated energy per surface area. By comparing the r distribution in the cohesive elements on Fig. 8 no element has undergone complete damage at u_{60}. Consequently, at this stage of the test, the load-displacement curve continues to exhibit a steady growth. Conversely, at point u_{80}, an initial set of elements becomes fully damaged, leading to an inflection point in the curve and subsequent smoothing. Additionally, it is observed that with the decrease in strength and the absence of load transfer between nodes, strains intensify in regions adjacent to the crack point. Then, the crack continues growing in point u_{90}, until point u_{100}, when the specimens fail.

In the model, the onset of cracks occurs simultaneously at identical loads for both corners of the overlapped area. However, in the experimental test, the onset of cracks initiates earlier on the right side of the specimen (the fixed arm in the test), attributable to manufacturing defects or variations in the experimental setup [65], but the results are quite similar.

4.2. Non-deterministic Validation

For the non-deterministic validation, a random sampling of 100 specimens has been conducted based on the statistical distributions of the variables summarized in Table 1 and a tolerance of 5% has been also defined as the criterion for validation. The results of the 100 simulations are henceforth referred to as the non-deterministic numerical results.

For the non-deterministic quantitative validation, the average curve and the $\pm 2\sigma$ interval for the non-deterministic numerical results are presented in Fig. 6. Additionally, the normalized average loads for the representative displacement points u_{60}, u_{80}, u_{90} and u_{100} and the average slope are summarized as non-deterministic values in Table 2. As can be seen for the dispersion of the non-deterministic results (represented by the bound of $\pm 2\sigma$), the behavior of the non-deterministic results is consistent with the nominal results and they fall below the maximum allowable threshold of 5% defined for the comparison with the experimental data.

The non-deterministic validation also covers the comparison between the distributions of the 2 batches of results studied, being the maximum admissible $\%d_{Area}$ less than 5%. Once the statistical parameters of τ_{SLS} distribution for each batch of results have been calculated, summarized in Table 3, the ECDF of the numerical and the experimental data have been calculated by the generation of 10^4 random points results based on the statistical parameters obtained, see Fig. 9, as described in Section 2.2.

Following the flowchart defined in Fig. 1, the non-deterministic validation of the M&S is carried out using Eq. (1); in this study we used the trapezoidal rule to approximate the integral to our ECDFs. The $\%d_{Area}$ obtained was 2.45% a value significantly below of 5%, the a-priori defined threshold. However, even with a small $\%d_{Area}$, our batches do not pass the hypothesis validation tests (see first row of Table 4), indicating that we are not in the 'scenario a' of Fig. 2.

Then, an offset equal to W_1 is applied in the numerical results to correct the small difference in location between the batches (resulting in a different scale parameter in the numerical 2-parameters Weibull distribution obtained in this case studied). After this correction, the p-value obtained in all the tests is higher than 0.05 (corresponding to 95% interval of confidence, see Table 4). Thus, inferring that the location of the distribution of τ_{SLS} for the M&S data, the similarity between M&S and experimental approaches can not be rejected for τ_{SLS} distributions with a 95% of confidence, confirming that we are in 'scenario b' of Fig. 2.

Therefore, based on the deterministic and non-deterministic analyses conducted between the M&S data and the experimental results, the M&S approach described in Section 2 is considered as a verified and validated approach for the generation of the τ_{SLS} allowable. Then, the B-value is calculated for the experimental and simulated cases as can be seen in Table 3 and Fig. 9. It is observed that the B-value predicted with the M&S approach is higher than the obtained from the experimental data, due to the batch size effect.

4.3. Batch Size effect

Once validation has been completed for the M&S approach, we aim to explore the possibilities of the methodology to reduce the number of simulations required, thereby minimizing computational costs, and explore the influence of the batch size on the prediction of the B-value. For each sample sizes described in Section 2.3, 10000 different combinations of data results have been generated.

The area method has been applied and the dispersion of results is represented in Fig. 10. The results show that when the batch size increases, the $\%d_{Area}$ is reduced between the ECDF of the experimental data and the ECDF of the numerical results selected. However, the reduction is not significant (less than 0.1%) for sizes bigger than 11 specimens. Only the dispersion is reduced but this is also an effect of the reduction in the possible combinations in the selection process of the data.

We have also checked how many of the combinations can be validated by each test for the batch sampling of 18, 30 50 and 70 as can be seen in Table 5. In general terms, the 99% of the batch of results passed the three tests for all the sizes checked. In addition, when the batch size is increased, more ECDF pass the validation test, indicating that follow the same distribution as the experimental one.

Then, the KDF was calculated using Equation Eq. (3)in function of each B-value generated as a function of the batch size and we present the results in Fig. 11. Comparing the behavior between sample size 6 and 11 it can be seen that the dispersion in the results affect significantly at the B-value obtained. The smaller dispersion of the experimental data for sampling generation in comparison to the M&S results affects positively to the B-value generated which has an average KDF higher than the numerically obtained. However, the KDF of the B-value increase with the sample size, and just with 18 numerical specimens the KDF is increased more than in the batch of 11 specimens (total experimental population). Thus, bigger batch sizes increase the KDF effect in the B-value. However, when the size of the sample increases enough, a plateau appears and the reduction in the dispersion is not even reduced.

5. Discussion

In the deterministic comparison the load displacement curve obtained for the M&S is aligned with the experimental results presented in Table 2, as it can be seen the error is small for the characteristic points studied. Qualitatively, the strain behaviour in both directions presents a similar behaviour. Being all the errors of the M&S lower than 5%, and having proved that the behaviour of the model is qualitatively acceptable, the M&S has been deterministically validated.

The comparison between the ECDFs also shows a good relation between the non-deterministic and the experimental results, locating the distributions in the 'scenario b'. Thus, the M&S approach for the DA generation has been validated. With the model validated, the B-value has been calculated and compared between the non-deterministic results generated in the DOE and the experimental data. The B-value obtained is similar. In addition, the size of the batch shows a large influence on the calculated B-value for small batch samples, where a plateau has been obtained when the sample size is 50. Consequently, the validated M&S approach can be used to complement the experimental test in generating the DA.

Finally, with the results obtained from the tests done to check the sampling size, it can be seen that 100 specimens are more than enough, for the case considered in this study. From the hypothesis validation it can be seen that with 50 simulated specimens, an optimal balance in the design allowable to computational time ratio is obtained.

6. Conclusions

This study successfully characterized the strength allowable of a single lap shear specimen manufactured with carbon fibre reinforced polymer thermoplastic-based laminate through both experimental testing and simulation.

The methodology to obtain the design allowable has been presented. Firstly, the modelling and simulation approach involving high fidelity model is defined. Afterwards, a validation strategy that covers both deterministic and non-deterministic approach for scenarios with similarity and dissimilarity in the distribution of the results has been defined. Once the model and simulation approach defined is validated, it is used to obtain the design allowable. The proposed numerical simulation, which uses a high-fidelity model based on 3D solid elements and an interface utilizing 3D cohesive elements, is capable of replicating the same behavior as the experimental single lap shear test selected in this study.

Moreover, through statistical comparisons of the distributions obtained, the influence of the sample size has been analyzed. The modeling and simulation approach has been validated for relatively small sample size (50 simulations for the current case study in this paper), which demonstrates the feasibility of the approach, to determine design allowables by simulation, with reasonable resources.

Acknowledgements

This work has been accomplished within the framework of an ongoing EU Horizon 2020 Clean Sky 2 Project TREAL (Thermoplastic material allowable generation using a reliability-based virtual modelling platform). This work has received funding from the Clean Sky 2 Joint Undertaking (JU) under grant agreement No. 864723. The JU receives support from the European Union's Horizon 2020 research and innovation programme and the Clean Sky 2 JU members other than the Union. The project consortium is formed by Amade-Universitat de Girona, Universidade do Porto, MSC e-Xstream, and the topic manager is Airbus Operations, France. This work has been partially funded by the Spanish Government (Ministerio de Ciencia e Innovación) under contract PID2021-127879OB-C21. AT acknowledges the Generalitat de Catalunya for the ICREA Academia prize 2022. Open Access funding provided thanks to the CRUE-CSIC, Spain agreement with Elsevier.

References

[1] J. C. Williams, E. A. Starke, Progress in structural materials for aerospace systems, Acta Materialia 51 (2003) 5775–5799. doi:10.1016/j.actamat.2003.08.023.

[2] S. W. Ghori, R. Siakeng, M. Rasheed, N. Saba, M. Jawaid, The role of advanced polymer materials in aerospace, in: Sustainable Composites for Aerospace Applications, Elsevier, 2018, pp. 19–34. doi:10.1016/B978-0-08-102131-6.00002-5.

[3] B. H. A. H. Tijs, M. H. J. Doldersum, A. Turon, C. Bisagni, Experimental and numerical evaluation of conduction welded thermoplastic composite joints, Composite Structures 281 (2022). doi:10.1016/j.compstruct.2021.114964.

[4] B. A. Alshammari, M. S. Alsuhybani, A. M. Almushaikeh, B. M. Alotaibi, A. M. Alenad, N. B. Alqahtani, A. G. Alharbi, Comprehensive review of the properties and modifications of carbon fiber-reinforced thermoplastic composites, Polymers 13 (2021). doi:10.3390/polym13152474, publisher: MDPI AG.

[5] F. N. Archibong, O. M. Sanusi, P. Médéric, N. Aït Hocine, An overview on the recycling of waste ground tyre rubbers in thermoplastic matrices: Effect of added fillers, Resources, Conservation and Recycling 175 (2021). doi:10.1016/j.resconrec.2021.105894, publisher: Elsevier B.V.

[6] W. Obande, C. M. Ó Brádaigh, D. Ray, Continuous fibre-reinforced thermoplastic acrylic-matrix composites prepared by liquid resin infusion – A review, Composites Part B: Engineering 215 (2021) 108771. URL: https://linkinghub.elsevier.com/retrieve/pii/S1359836821001633. doi:10.1016/j.compositesb.2021.108771.

[7] T. Zhao, G. Palardy, I. F. Villegas, C. Rans, M. Martinez, R. Benedictus, Mechanical behaviour of thermoplastic composites spot-welded and mechanically fastened joints: A preliminary comparison, Composites Part B: Engineering 112 (2017) 224–234. doi:10.1016/j.compositesb.2016.12.028, publisher: Elsevier Ltd.

[8] L. C. M. Barbosa, D. B. Bortoluzzi, A. C. Ancelotti, Analysis of fracture toughness in mode II and fractographic study of composites based on Elium® 150 thermoplastic matrix, Compos-

ites Part B: Engineering 175 (2019). doi:10.1016/j.compositesb.2019.107082, publisher: Elsevier Ltd.

[9] S. Sieberer, C. Savandaiah, S. Pichler, J. Maurer, M. Schagerl, Influence of post-consolidation on continuous carbon-fibre reinforced additively manufactured specimens in bending, Composite Structures 320 (2023) 117176. URL: https://linkinghub.elsevier.com/retrieve/pii/S0263822323005202. doi:10.1016/j.compstruct.2023.117176.

[10] Chapter 8 - Building Block Approach, in: B. Backman (Ed.), Composite Structures, Design, Safety and Innovation, Elsevier, Oxford, 2005, pp. 99–110. URL: www.sciencedirect.com/science/article/pii/B9780080445458500085. doi:10.1016/B978-008044545-8/50008-5.

[11] CMH-17 organization, Composite Materials Handbook - Vol. 1 Polymer Matrix Composites Guidelines for Characterisation of Structural Materials, volume 1, 2002. Publication Title: Composite Materials Handbook 17 Series Issue: June.

[12] Clean Aviation, Strategic Research and Innovation Agenda of the Clean Aviation Joint Undertaking, Technical Report, Clean Aviation, 2021.

[13] O. Vallmajó, I. Cózar, C. Furtado, R. Tavares, A. Arteiro, A. Turon, P. Camanho, Virtual calculation of the B-value allowables of notched composite laminates, Composite Structures 212 (2019) 11–21. URL: https://linkinghub.elsevier.com/retrieve/pii/S0263822318345318. doi:10.1016/j.compstruct.2018.12.049.

[14] C. Furtado, L. F. Pereira, R. P. Tavares, M. Salgado, F. Otero, G. Catalanotti, A. Arteiro, A methodology to generate design allowables of composite laminates using machine learning, International Journal of Solids and Structures (2020) 16. doi:10.1016/j.ijsolstr.2021.111095.

[15] K. Nam, K. J. Park, S. J. Shin, S. J. Kim, I.-H. Choi, Estimation of composite laminate design allowables using the statistical characteristics of lamina level test data, International Journal of Aeronautical and Space Sciences 16 (2015) 360–369. doi:10.5139/IJASS.2015.16.3.360, publisher: Korean Society for Aeronautical and Space Sciences.

[16] G. Catalanotti, Uncertainty quantification for advanced progressive damage models for composites by means of efficient emulators and bootstrapping, Composites Part A: Applied Science and Manufacturing 163 (2022) 107238. URL: https://linkinghub.elsevier.com/retrieve/pii/S1359835X22004195. doi:10.1016/j.compositesa.2022.107238, publisher: Elsevier Ltd.

[17] I. Cózar, A. Turon, E. González, O. Vallmajó, A. Sasikumar, A methodology to obtain material design allowables from high-fidelity compression after impact simulations on composite laminates, Composites Part A: Applied Science and Manufacturing 139 (2020) 106069. URL: https://linkinghub.elsevier.com/retrieve/pii/S1359835X20303080. doi:10.1016/j.compositesa.2020.106069, publisher: Elsevier Ltd.

[18] D. C. O'Mahoney, K. B. Katnam, N. P. O'Dowd, C. T. McCarthy, T. M. Young, Taguchi analysis of bonded composite single-lap joints using a combined interface-adhesive damage model, International Journal of Adhesion and Adhesives 40 (2013) 168–178. doi:10.1016/j.ijadhadh.2012.06.001, publisher: Elsevier Ltd.

[19] J. A. Neto, R. D. Campilho, L. F. Da Silva, Parametric study of adhesive joints with composites, in: International Journal of Adhesion and Adhesives, volume 37, 2012, pp. 96–101. doi:10.1016/j.ijadhadh.2012.01.019, iSSN: 01437496.

[20] X. Han, Y. Jin, L. F. M. Da Silva, M. Costa, C. Wu, On the effect of adhesive thickness on mode I fracture energy - an experimental and modelling study using a trapezoidal cohesive zone model, Journal of Adhesion 96 (2020) 490–514. doi:10.1080/00218464.2019.1601087, publisher: Taylor and Francis Inc.

[21] B. H. A. H. Tijs, S. Abdel-Monsef, J. Renart, A. Turon, C. Bisagni, Characterization and analysis of the interlaminar behavior of thermoplastic composites considering fiber bridging and R-curve effects, Composites Part A (2022). URL: https://doi.org/10.1016/j.compositesa.2022.107101.

[22] J. Fatemi, G. Poort, Re-engineering the engineering processes for space product development, 16th ECSSMET, 2021.

[23] S. Riedmaier, B. Danquah, B. Schick, F. Diermeyer, Unified Framework and Survey for Model Verification, Validation and Uncertainty Quantification, Archives of Computational Methods in Engineering 28 (2021) 2655–2688. doi:10.1007/s11831-020-09473-7, publisher: Springer Science and Business Media B.V.

[24] C. R. Hicks, Fundamental concepts in the design of experiments, 1964.

[25] R. Snee, The Statistical Approach to Design of Experiments (Chapter 5), in: Perspectives on Contemporary Statistics, The Mathematical Association of America, 1992. URL: https://www.researchgate.net/publication/283082880.

[26] F. Pukelsheim, Optimal design of experiments, SIAM, 2006. URL: https://epubs.siam.org/terms-privacy.

[27] L. F. Da Silva, T. N. Rodrigues, M. A. Figueiredo, M. F. de Moura, J. A. Chousal, Effect of adhesive type and thickness on the lap shear strength, Journal of Adhesion 82 (2006) 1091–1115. doi:10.1080/00218460600948511.

[28] L. F. M. Da Silva, G. W. Critchlow, M. A. Figueiredo, Parametric study of adhesively bonded single lap joints by the taguchi method, in: Journal of Adhesion Science and Technology, volume 22, 2008, pp. 1477–1494. doi:10.1163/156856108X309585, issue: 13 ISSN: 01694243.

[29] H. Rangaswamy, I. Sogalad, S. Basavarajappa, S. Acharya, G. C. Manjunath Patel, Experimental analysis and prediction of strength of adhesive-bonded single-lap composite joints: Taguchi and artificial neural network approaches, SN Applied Sciences 2 (2020). doi:10.1007/s42452-020-2851-8, publisher: Springer Nature.

[30] S. Joannès, F. Islam, L. Laiarinandrasana, Uncertainty in Fibre Strength Characterisation Due to Uncertainty in Measurement and Sampling Randomness, Applied Composite Materials 27 (2020) 165–184. doi:10.1007/s10443-020-09803-9, publisher: Springer.

[31] W. Tao, P. Zhu, C. Xu, Z. Liu, Uncertainty quantification of mechanical properties for three-dimensional orthogonal woven composites. Part II: Multiscale simulation, Composite Structures 235 (2020). doi:10.1016/j.compstruct.2019.111764, publisher: Elsevier Ltd.

[32] H. Zhang, L. Zhang, Z. Song, P. Zhu, Hierarchical uncertainty quantification of hybrid (riveted/bonded) single lap aluminum-CFRP joints with structural multiscale characteristic, Composite Structures 324 (2023). doi:10.1016/j.compstruct.2023.117561.

[33] G. Catalanotti, Navigating the unknown: Tackling high-dimensional challenges in composite damage modeling with bootstrapping and Bayesian uncertainty quantification, Composites Science and Technology 248 (2024) 110462. URL: https://linkinghub.elsevier.com/retrieve/pii/S0266353824000320. doi:10.1016/j.compscitech.2024.110462.

[34] A. Ciampaglia, Data driven statistical method for the multiscale characterization and modelling of fiber reinforced composites, Composite Structures 320 (2023). doi:10.1016/j.compstruct.2023.117215, publisher: Elsevier Ltd.

[35] J. Fatemi, G. Poort, Towards qualification of composite launcher structures by simulation, 17th ECSSMET, 2023.

[36] G. Poort, J. Fatemi, Qualification of the Vega-C Inter-stage 1/2 Structure by Simulation, 16th ECSSMET, 2021.

[37] C. J. Roy, W. L. Oberkampf, A comprehensive framework for verification, validation, and uncertainty quantification in scientific computing, Computer Methods in Applied Mechanics and Engineering 200 (2011) 2131–2144. doi:10.1016/j.cma.2011.03.016, publisher: Elsevier B.V.

[38] J. L. J. Hodges, The Significance Probability of the Smirnov Two-Sample Test, Arkiv fiur Matematik 3 (1958) 469–486.

[39] F. W. Scholz, M. A. Stephens, K-Sample Anderson-Darling Tests, Journal of the American Statistical Association 82 (1987) 918–924.

[40] T. W. Anderson, On the Distribution of the Two-Sample Cramer-von Mises Criterion, The Annals of Mathematical Statistics 33 (1962) 1148–1159. doi:10.1214/aoms/1177704477.

[41] B. Wang, X. Ma, P. Hao, Y. Sun, K. Tian, G. Li, K. Zhang, L. Jiang, J. Guo, Improved knock-down factors for composite cylindrical shells with delamination and geometric imperfections, Composites Part B: Engineering 163 (2019) 314–323. URL: https://linkinghub.elsevier.com/retrieve/pii/S1359836818323965. doi:10.1016/j.compositesb.2018.11.049.

[42] R. Degenhardt, A. Kling, A. Bethge, J. Orf, L. Kärger, R. Zimmermann, K. Rohwer, A. Calvi, Investigations on imperfection sensitivity and deduction of improved knock-down factors for unstiffened CFRP cylindrical shells, Composite Structures 92 (2010) 1939–1946. URL: https://linkinghub.elsevier.com/retrieve/pii/S0263822309005273. doi:10.1016/j.compstruct.2009.12.014.

[43] T. J. DiCiccio, B. Efron, Bootstrap confidence intervals, Statistical Science 11 (1996) 189–212. Publisher: Institute of Mathematical Statistics ISBN: 08834237.

[44] AITM 1-0019: Determination of Tensile Lap Shear Strength of Composite Joints, Technical Report, 2017.

[45] A. Redmann, V. Damodaran, F. Tischer, P. Prabhakar, T. A. Osswald, Evaluation of single-lap and block shear test methods in adhesively bonded composite joints, Journal of Composites Science 5 (2021). doi:10.3390/jcs5010027, publisher: MDPI AG.

[46] H. Osnes, A. Andersen, Computational analysis of geometric nonlinear effects in adhesively bonded single lap composite joints, Composites Part B: Engineering 34 (2003) 417–427. doi:10.1016/S1359-8368(03)00023-4, publisher: Elsevier Ltd.

[47] R. Bigger, B. Blaysat, C. Boo, M. Grewer, J. Hu, A. Jones, M. Klein, K. Raghavan, P. Reu, T. Schmidt, T. Siebert, M. Simenson, D. Turner, A. Vieira, T. Weikert, A Good Practices Guide for Digital Image Correlation, International Digital Image Correlation Society, 2018. doi:10.32720/idics/gpg.ed1.

[48] Dassault Systèmes Simulia Corp., Abaqus, 2022.

[49] A. Turon, E. V. González, C. Sarrado, G. Guillamet, P. Maimí, Accurate simulation of delamination under mixed-mode loading using a cohesive model with a mode-dependent penalty stiffness, Composite Structures 184 (2018) 506–511. doi:10.1016/j.compstruct.2017.10.017.

[50] A. Turon, C. G. Dávila, P. P. Camanho, J. Costa, An engineering solution for mesh size effects in the simulation of delamination using cohesive zone models, Engineering Fracture Mechanics 74 (2007) 1665–1682. doi:10.1016/j.engfracmech.2006.08.025.

[51] A. Soto, E. V. González, P. Maimí, A. Turon, J. R. Sainz de Aja, F. M. de la Escalera, Cohesive zone length of orthotropic materials undergoing delamination, Engineering Fracture Mechanics 159 (2016) 174–188. doi:10.1016/j.engfracmech.2016.03.033, publisher: Elsevier Ltd.

[52] ASTM D3039/D3039M: Standard Test Method for Tensile Properties of Polymer Matrix Composite Materials, Technical Report, 2018. doi:10.1520/D3039_D3039M-17.

[53] ASTM D3518/D3518M: Standard Test Method for In-Plane Shear Response of Polymer Matrix Composite Materials by Tensile Test of a ±45° Laminate, Technical Report, 2018. doi:10.1520/D3518_D3518M-18.

[54] ASTM D6671/D6671M: Standard Test Method for Mixed Mode I-Mode II Interlaminar Fracture Toughness of Unidirectional Fiber Reinforced Polymer Matrix Composites 1, Technical Report, 2022. URL: www.astm.org. doi:10.1520/D6671_D6671M-22.

[55] ISO 15024:2023(E): Fibre-reinforced plastic composites - Determination of mode I interlaminar fracture toughness, GIc, for unidirectionally reinforced materials, Technical Report, International Organitzation of Standaritzation, Switzerland, 2023. URL: www.iso.org/standard/84263.html.

[56] ISO 15114:2014(E): Fibre-reinforced plastic composites — Determination of the mode II fracture resistance for unidirectionally reinforced materials using the calibrated end-loaded split (C-ELS) test and an effective crack length approach, Technical Report, International Organitzation of Standaritzation, Switzerland, 2014. URL: https://www.iso.org/standard/55357.html.

[57] S. Abdel-Monsef, A. Ortega, A. Turon, P. Maimí, J. Renart, An efficient method to extract a mode I cohesive law for bonded joints using the double cantilever beam test, Composites Part B: Engineering 178 (2019) 107424. doi:10.1016/j.compositesb.2019.107424, publisher: Elsevier Ltd.

[58] S. Abdel-Monsef, M. Pérez-Galmés, J. Renart, A. Turon, P. Maimí, The influence of mode ll test configuration on the cohesive law of bonded joints, Composite Structures 234 (2020). doi:10.1016/j.compstruct.2019.111689.

[59] E. V. González, P. Maimí, P. P. Camanho, A. Turon, J. A. Mayugo, Simulation of drop-weight impact and compression after impact tests on composite laminates, Composite Structures 94 (2012) 3364–3378. doi:10.1016/j.compstruct.2012.05.015.

[60] I. R. Cózar, F. Otero, P. Maimí, E. V. González, S. Miot, A. Turon, P. P. Camanho, A three-dimensional plastic-damage model for polymer composite materials, Composites Part A: Applied Science and Manufacturing 163 (2022). doi:10.1016/j.compositesa.2022.107198, publisher: Elsevier Ltd.

[61] I. R. Cózar, J. J. Arbeláez-Toro, P. Maimí, F. Otero, E. V. González, A. Turon, P. P. Camanho, A novel methodology to measure the transverse Poisson's ratio in the elastic and plastic regions for composite materials, Composites Part B: Engineering 272 (2024). doi:10.1016/j.compositesb.2023.111098, publisher: Elsevier Ltd.

[62] Department of Defense / U.S.A., Composite Materials Handbook - Vol. 3 Polymer Matrix Composites Materials Usage, Design, and Analysis, volume 3, 2002. Publication Title: Composite Materials Handbook 17 Series.

[63] I. Paliwal, M. Ramji, A detailed study on the damage evolution and failure assessment of single-lap hybrid joints in CFRP laminates under tensile loading, Composite Structures 299 (2022). doi:10.1016/j.compstruct.2022.116021, publisher: Elsevier Ltd.

[64] Z. He, Q. Luo, Q. Li, G. Zheng, G. Sun, Fatigue behavior of CFRP/Al adhesive joints — Failure mechanisms study using digital image correlation (DIC) technique, Thin-Walled Structures 174 (2022). doi:10.1016/j.tws.2022.109075, publisher: Elsevier Ltd.

[65] S. Wang, W. Liang, L. Duan, G. Li, J. Cui, Effects of loading rates on mechanical property and failure behavior of single-lap adhesive joints with carbon fiber reinforced plastics and aluminum alloys, International Journal of Advanced Manufacturing Technology 106 (2020) 2569–2581. doi:10.1007/s00170-019-04804-w, publisher: Springer.

[66] P. Virtanen, R. Gommers, T. E. Oliphant, M. Haberland, T. Reddy, D. Cournapeau, E. Burovski, P. Peterson, W. Weckesser, J. Bright, S. J. Van Der Walt, M. Brett, J. Wilson, K. J. Millman, N. Mayorov, A. R. J. Nelson, E. Jones, R. Kern, E. Larson, C. J. Carey, Polat, Y. Feng, E. W. Moore, J. VanderPlas, D. Laxalde, J. Perktold, R. Cimrman, I. Henriksen, E. A. Quintero, C. R. Harris, A. M. Archibald, A. H. Ribeiro, F. Pedregosa, P. Van Mulbregt, SciPy 1.0 Contributors, SciPy 1.0: fundamental algorithms for scientific computing in Python, Nature Methods 17 (2020) 261–272. URL: https://www.nature.com/articles/s41592-019-0686-2. doi:10.1038/s41592-019-0686-2.

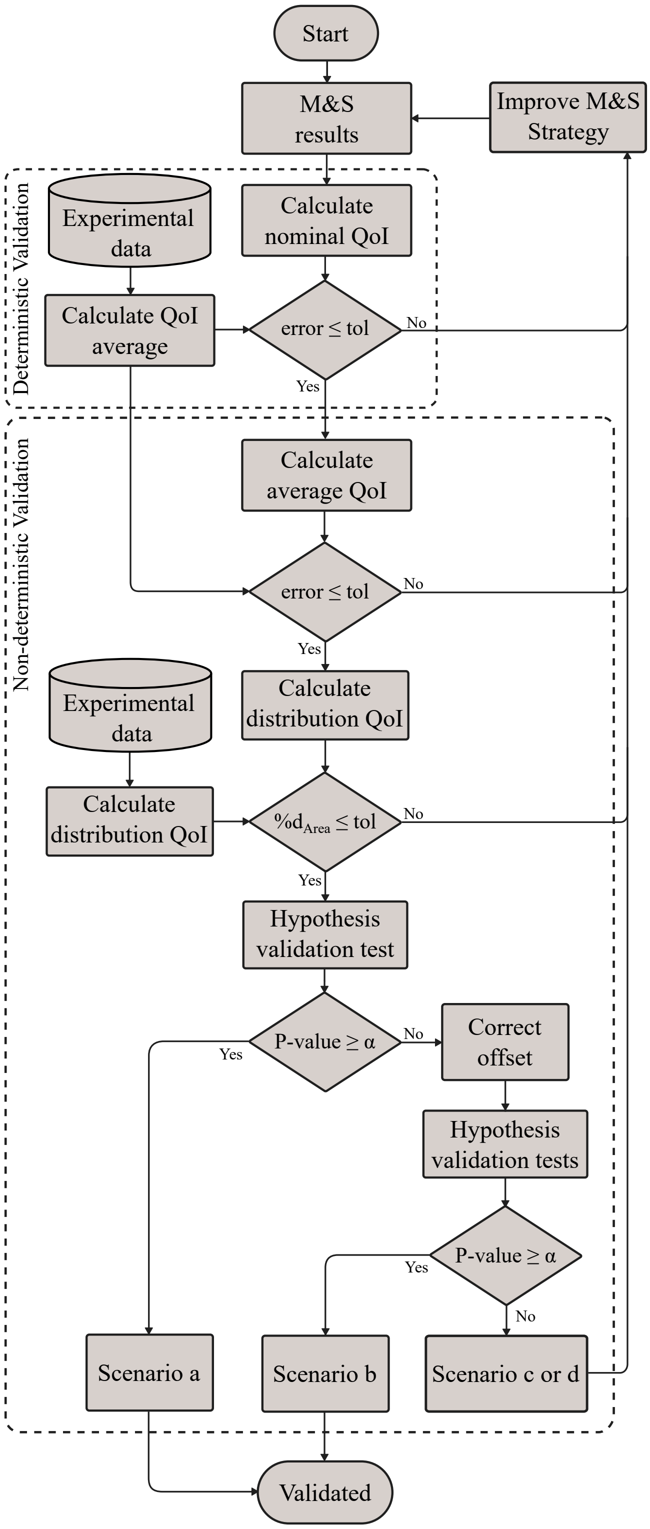

Figure 1. Flow chart of the validation process, where α is the p-value of the defined confidence interval. The scenarios are presented in Fig. 2.

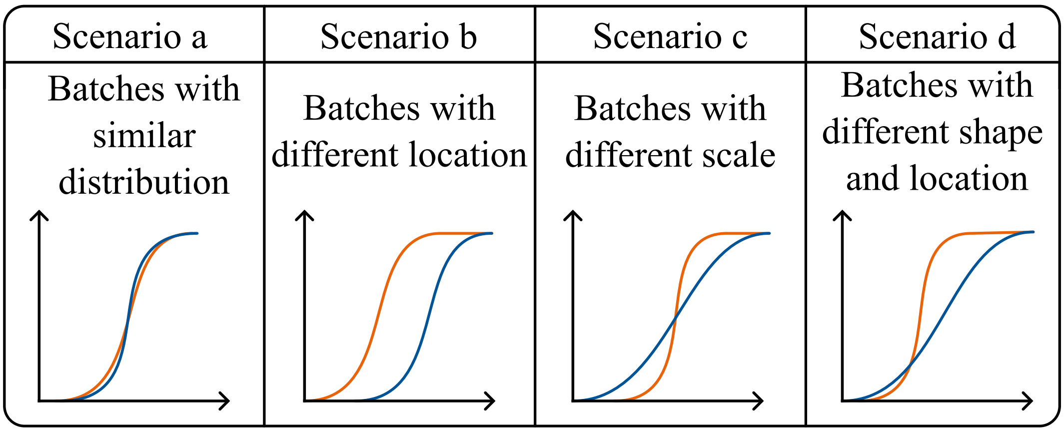

Figure 2. Schematic representation of the CDF comparison, for similarity and discrepancies in the location and/or scale.

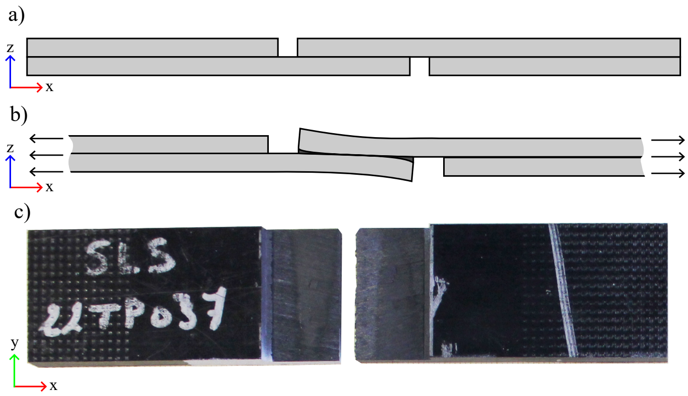

Figure 3. a) SLS specimen geometry, b) loading conditions and deformed shape of the specimen during the experimental test and c) specimen broken after test.

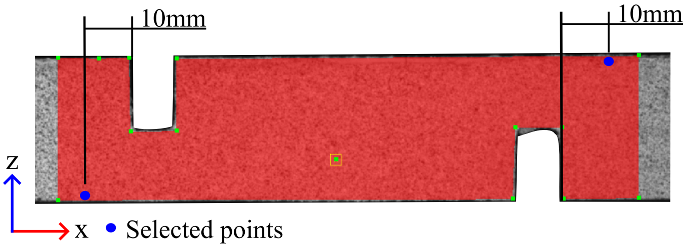

Figure 4. Studied area in the DIC software.

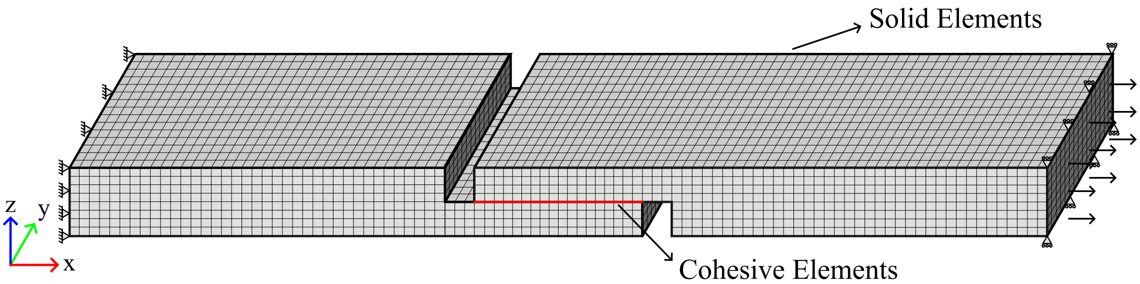

Figure 5. Schematic representation of the model geometry, mesh and boundary conditions applied in the HFM.

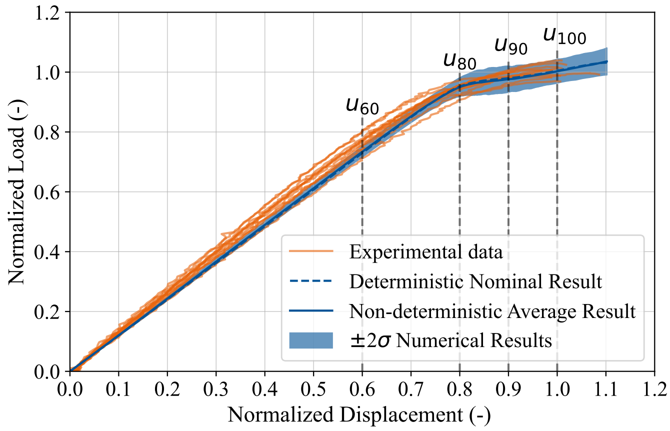

Figure 6. Normalized load-displacement curves for experimental SLS test and the HFM with average values for the input parameters.

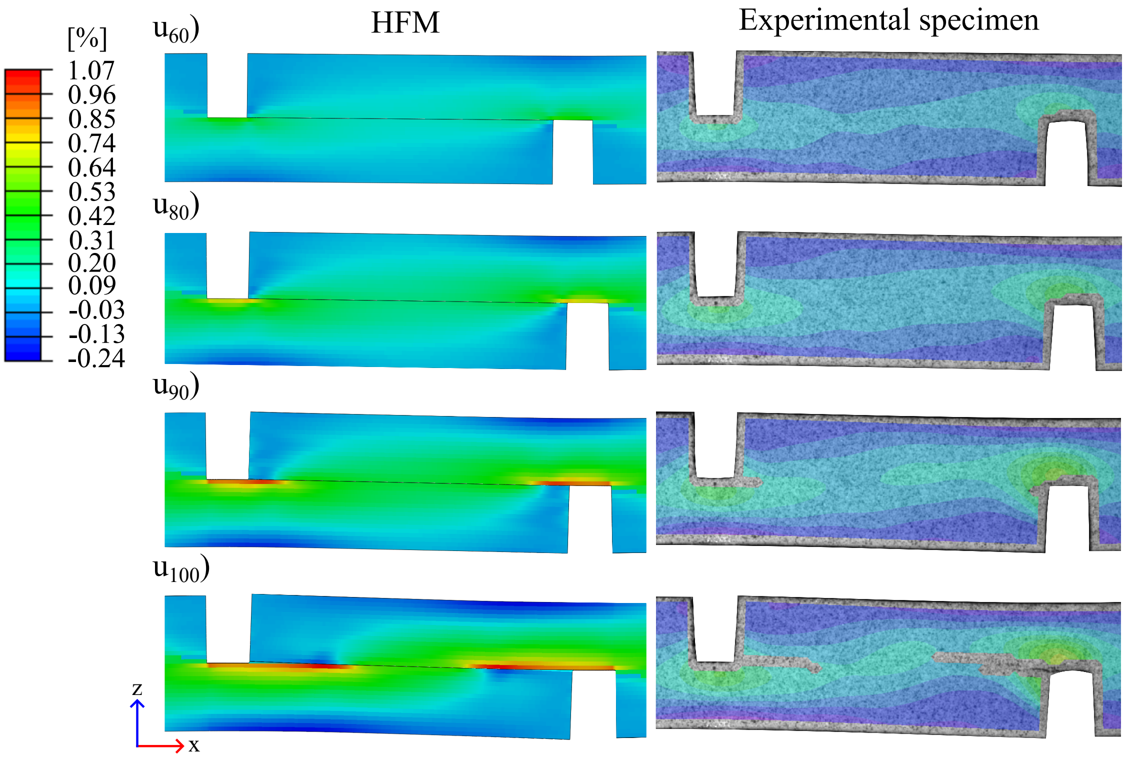

Figure 7. Logarithmic strains contour in length direction (x-axis) comparison between the nominal HFM and a experimental specimen during the test at u_{60}, u_{80}, u_{90} and u_{100}.

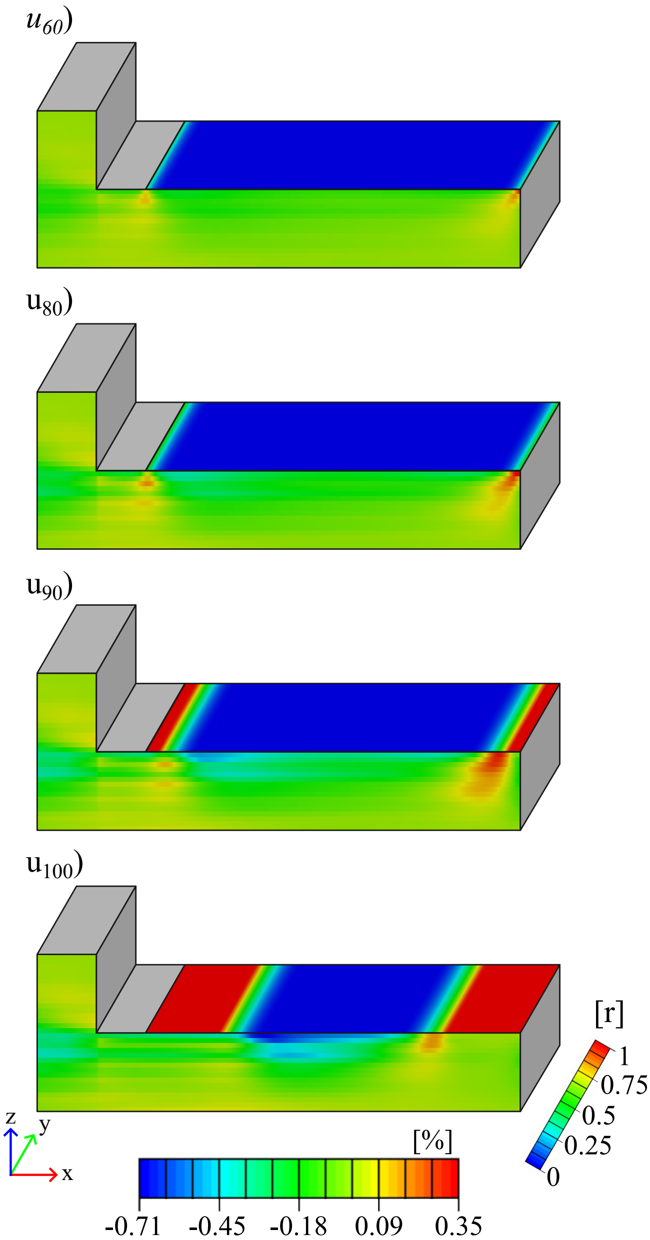

Figure 8. Logarithmic strains contour in thickness direction (z-axis) in the front face and damage (r) in the cohesive surface (from 0 no damage until 1 fully damage) for the nominal HFM specimen during the test at u_{60}, u_{80}, u_{90} and u_{100}.

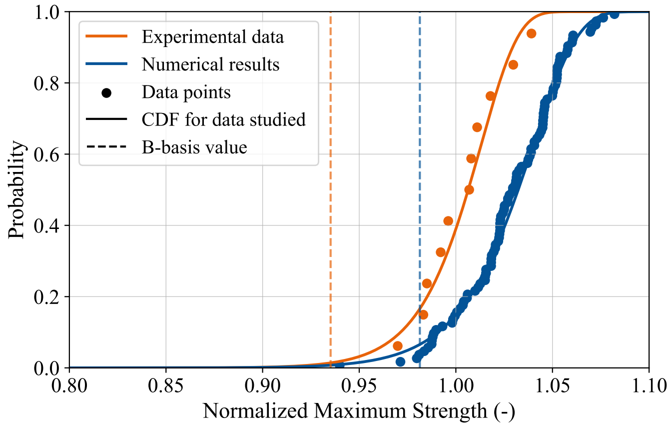

Figure 9. ECDF for n=10000 fitted for the failure strength data, B-value for the experimental data and numerical results.

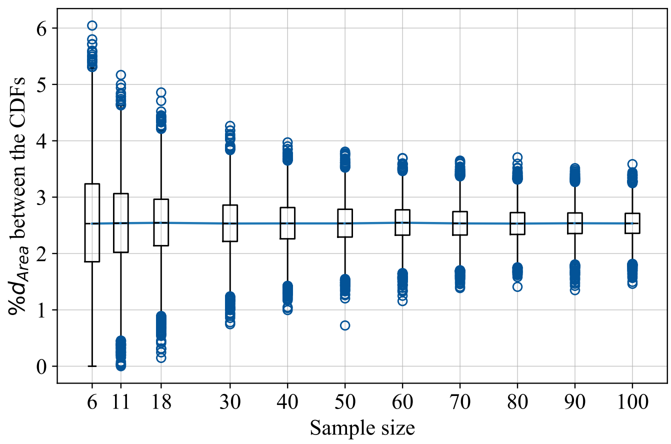

Figure 10. $\%d_{Area}$ between ECDF of the experimental τ_{SLS} and for the numerical samples selected in function of the size.

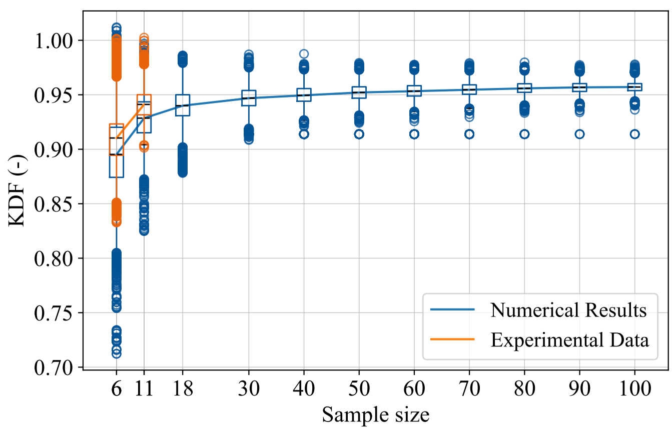

Figure 11. Comparison of the KDF dispersion between the HFM and the experimentally obtained with respect to the sample size.

Table 1. Material properties experimentally obtained for the AS7/PEKK used in the HFM. [1] Scale of each material property is normalized by dividing it by the average value of that property across all materials

Material Properties	Test	Data Reduction Method	Num. Samples	Distribution	Scale [1]	Shape
E_{11} (MPa)	Longitudinal Tensile (0^{o})	ASTM D3039 [52]	18	Weibull	1.01 (-)	86.87
E_{22} (MPa)	Transverse Tensile (90^{o})	ASTM D3039 [52]	6	Weibull	1.00 (-)	194.4
ν_{12}	Longitudinal Tensile (0^{o})	ASTM D3039 [52]	18	Weibull	1.03 (-)	15.32
G_{12} (MPa)	In-Plane Shear	ASTM D3518M [53]	12	Weibull	1.00 (-)	114.9
$\mathcal{G}_{c1}$ (J/m^2)	Double Cantilever Beam	ISO 15024 [55]	12	Weibull	1.01 (-)	44.27
$\mathcal{G}_{c2}$ (J/m^2)	End Loaded Split	ISO 15114 [56]	12	Weibull	1.05 (-)	20.67
η	Mixed-mode	ASTM D6671 [54]	6	Weibull	1.06 (-)	9.64
τ_I (MPa)	Double Cantilever Beam	Said et al. [57]	12	Weibull	1.05 (-)	9.82
τ_{II} (MPa)	End Loaded Split	Said et al. [58]	12	Weibull	1.02 (-)	21.79

Table 2. Average values for normalized slope and loads at displacement points u_{60}, u_{80}, u_{90} and u_{100} and error between experimental average values and numerically predicted.

	Slope of elastic region	u_{60}	u_{80}	u_{90}	u_{100}
Experimental	1.25 (-)	0.77 (-)	0.95 (-)	0.99 (-)	1.00 (-)
Deterministic nominal result	1.22 (-)	0.73 (-)	0.95 (-)	0.98 (-)	1.03 (-)
Non-deterministic average result	1.22 (-)	0.73 (-)	0.95 (-)	0.99 (-)	1.03 (-)
Err. Deterministic	2.38%	4.46%	0.99%	0.52%	2.80%
Err. Non-deterministic	2.14%	4.26%	0.56%	0.91%	2.48%

Table 3. Metric comparison for the non-deterministic validation. [2] Results for each approach is normalized by dividing it by the average value of the experimental data

Case	Size	Average [2]	B-value	Distribution	Scale	Shape
Experimental data	11	1.00 (-)	0.932 (-)	Weibull	1.010 (-)	53.18
M&S results	100	1.03 (-)	0.981 (-)	Weibull	1.040 (-)	45.92

Table 4. P-value from the statistical tests assessed for the experimental and non-deterministic results. [3] P-value calculation stops in 0.25 for Anderson-Dawing in Scipy [66]

Case	KV	AD	CV
without correction	0.003	0.003	0.002
with offset W_1 applied	0.962	0.250[3]	0.855

Table 5. Percentage of batches which their distribution passed the statistical tests KS, AD and CV.

Test	Number of specimens 18	30	50	70
KS	99.63	99.86	100	100
AD	99.69	99.93	100	100
CV	99.69	99.89	100	100